Pulsatile pressure actuation enhances solute clearance in engineered vasculature through strain accumulation–release

Daniel Alcaide[1,2,3], A. Bancaud[1,3,4], J. Cacheux[1,3,4]*, Y.T. Matsunaga[1,2,3]*

1 – Institute of Industrial Science, The University of Tokyo, 4-6-1 Komaba, Meguro-ku, 153-8505 Tokyo, Japan

2 – Department of Bioengineering, School of Engineering, The University of Tokyo, 4-6-1 Komaba, Meguro-ku, 153-8505 Tokyo, Japan

3 – LIMMS, CNRS-IIS UMI 2820, The University of Tokyo, 153-8505 Tokyo, Japan

4 – LAAS-CNRS, CNRS UPR8001, 7 Avenue du Colonel Roche, 31400 Toulouse, France

* correspondence

Abstract (185 words)

Tissue homeostasis depends critically on the exchange of interstitial fluid between blood and tissues, as well as lymphatic drainage. While mechanical forces, such as external compression during physical activity, are known to accelerate interstitial fluid clearance, arterial pulsatility is hypothesized to play a similar role, especially in regions lacking lymphatic vasculature, such as the central nervous system. Here, we investigate how vascular pulsations modulate solute transport using a novel multi-microvessel pulsatile interstitial flow (PIF) chip. This platform enables real-time visualization of deformation and solute dynamics within a tissue-mimetic collagen hydrogel. Our results reveal a clipped Gent-like porohyperelastic response in acellular lumens, which is further amplified in vascularized lumens exhibiting asymmetric expansion-retraction behavior. Notably, microvessels induce strain retention within the hydrogel bulk, which is abruptly released during each pressure cycle. This cyclic strain retention and release mechanism coincides with a 1.3-fold increase in solute velocity, accelerating tracer clearance under pulsatile actuation compared to constant pressure. These findings highlight a vasculature-driven transport mechanism, where deformation-induced flow enhances interstitial clearance. These results provide new insights into how vascular dynamics may contribute to tissue homeostasis and interstitial fluid clearance.

INTRODUCTION

Homeostasis is the ability of the body to maintain a stable internal environment, ensuring proper function at both the cellular and organ levels. This stability is achieved through tightly regulated physiological mechanisms that continuously adjust tissue interstitial fluid (IF) volume and composition. Fluid exchanges between blood and surrounding tissues are generally described by the Starling principle[1], which assumes an equilibrium between the convective flow through the blood endothelium driven by blood pressure opposed to the oncotic pressure, the osmotic pressure resulting from the difference in proteins concentration between blood and tissue IF. In most tissues, this balance also includes the contribution of the lymphatic system that drains the IF and conveys it back into the blood circulatory system[2,3].

Other processes, which are based on mechanical stimulation, have been shown to contribute to IF drainage. Massage applies rhythmic compression and release to tissues, and enhances IF evacuation. It is commonly performed to reduce IF overload in limbs in *e.g.*, the context of lymphedema treatment[4]. A similar mechanism of evacuation has been documented during exercise. The intrinsic deformation occurring in muscles compresses interstitial spaces and enhances IF evacuation toward lymphatics or venules[5]. Last, the vascular system is periodically deformed as a consequence of heartbeat. This pulsatile deformation is known to be an important part of the brain's overall waste clearance system. In this organ where the lymphatic vasculature is absent, periodic deformation of the arteries have been shown to induce a fluid flow in the periarterial space, giving birth to what we now know as the glymphatic system[6]. According to the glymphatic model, arterial pulsations are suspected to also induce bulk IF displacements in the brain, *i.e.*, in the arteries' radial direction[7]. However, the characterization of this IF flow *in vivo* remains an unresolved technical challenge[8]. Common approaches couple data such as MRI imaging with IF flow modeling to infer parameters such as fluid velocity cannot be made directly, leaving space for strong controversies about the physical mechanisms behind glymphatic IF recirculation[9,10].

The consequences of pulsating loads on the transport of solutes in soft and permeable tissues have been extensively studied using cartilage[11–14], which naturally experiences physiological mechanical stimulation during walking. In as much as in soft porous hydrogels[15,16], enhanced dispersion of large solutes has been consistently reported. As supported by analytical[17] and numerical models[18], the enhanced dispersion is accounted for by (i) analogously to Taylor dispersion in a tube[19,20], the solid velocity profile in the pores spreads out concentration fronts along the flow direction much faster than normal diffusion, and (ii) the morphology of the pore

structure that introduces variability in the fluid streamlines and induces longitudinal and transverse spreading[21]. Despite this consensus, the translation of these conclusions into actual readouts for pulsation-based enhanced recirculation remains challenging, as tissues are associated to endothelial barriers, and thus form a composite material with heterogeneous transport properties. The solute transport regime induced by periodic pressure actuation likely reflects more than the linear combination of the permeability and elasticity of the barrier and the tissue.

We therefore aimed to fill this gap in understanding of pulsation-driven solute transport across endothelial barriers by setting up an *in vitro* model using tissue engineering approaches. We fabricated a pulsatile interstitial flow-on-chip (PIF chip), which consists in three parallel and coplanar cylindrical channels running through a collagen hydrogel matrix. This scaffold was used either acellularly by itself (Fig. 1A, upper panels) or vascularized with human umbilical vein endothelial cells (HUVECs) seeded into the two lateral channels to form microvessels (MVs), while the central channel was always kept acellular (Fig. 1A, lower panels) to enable efficient injection of fluorescent probes for tracking solute transport within the extracellular matrix. The PIF chip additionally facilitated the monitoring of solid-matrix deformation by quantifying acellular and vascularized lumen deformation in response to periodic or constant pressure. We proceed to first examine the deformation of a single channel and demonstrated the localization of the deformation induced by the barrier function of endothelial cell monolayers. Following, PIF multiple lumen and collagen gel bulk deformation dynamics are documented, intending to establish a link between deformation and solute transport within the devices. Solute transport analysis reveals that constant and pulsatile pressures yield equivalent transport in acellular PIF, but the vascularization breaks this equivalency through the induction of rapid MV expansion as well as the accumulation and transient release of strain in hydrogels during each pulsation. These mechanical effects appear to coincide with enhanced tracer displacements, in turn accounting for the increased solute clearance though the central injection channel detected with pulsatile pressure. We finally recapitulate this data and discuss its potential implications for molecular exchanges in tissues.

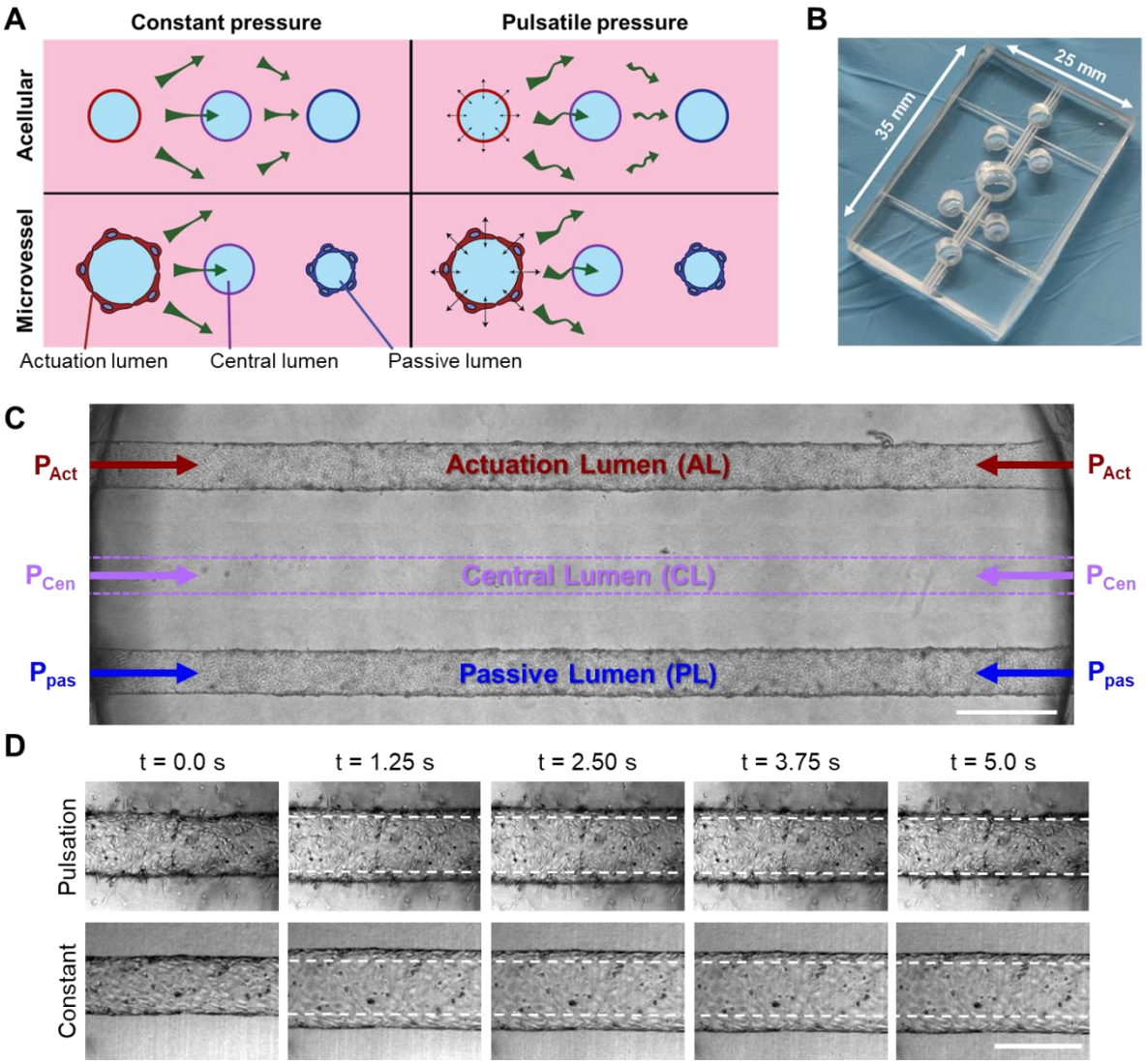

Figure 1 – Pulsatile Interstitial Flow-on-chip (PIF chip). **(A)** Cross-section of the acellular or vascularized system with the two scenarios of hydrodynamic actuation. Green arrows and thin black arrows represent the interstitial flow and the periodic actuation, respectively. **(B)** Photograph of the PIF chip with its dimensions. **(C)** Vascularized PIF chip panoramic bright field micrograph. MVs are fabricated in the lateral channels, while the central one is left acellular for tracer injection. Scale bar = 400 µm. **(D)** Actuation MV bright field snippets under pulsatile sinusoidal pressure (top panels) and constant pressure (bottom panels). Dashed lines indicate MV diameter at t = 0 s. Scale bar = 300 µm.

RESULTS

PIF device design and operation

PIF device design drew inspiration from standard 3D MV systems fabricated with 200 µm diameter acupuncture needles[22]. It was fabricated using laser etching and ablation of two silicone sheets (see Methods) that were then bonded by thermal annealing following oxygen-plasma surface activation Fig. 1B and Sup. Fig. 1A-D). The main cylindrical chamber that contains the collagen gel measured 5 mm in diameter in order to host three coplanar parallel acupuncture needles separated 500 µm from each other. The collagen solution was poured in the main chamber with the needles in place. After reticulation, needles were withdrawn and the platform was functional in acellular settings or with MVs upon HUVEC seeding (Fig. 1C and Suppl. Fig. 1E). In the following, we designate the channel under pressure as the *actuation lumen* (AL), the opposite lateral lumen being the *passive lumen* (PL), and one in between as the *central lumen* (CL, Fig. 1C).

Pressure regulation within each lumen was achieved using a custom biocompatibilized 3D-printed device placed on top of the silicon chip (see Methods and Suppl. Fig. 2), which allowed us to control the pressure in the AL, PL, and CL as well as on top of the collagen chamber. The pressure settings were typically defined by a baseline pressure of 100 Pa in PL, CL and on top of the chamber, and either a sinusoidal pressure input (5 s period, 100–900 Pa) or a constant pressure of 500 Pa in AL. Pulse period was selected to ensure faithful actuation by the digital pressure actuator and, because we are dealing with a bulk material softer than real tissue, a time-scale larger than heartbeat is required to force poroelastic consolidation[23,24] (see more below). Inspection of the deformation of AL by bright field microscopy showed that pulsatile pressure actuation induced periodic diameter changes of AL, whereas constant pressure expectedly maintained the actuating channels expanded (Fig 1D).

MVs localize the interstitial pore pressure gradient and the resulting strain

To evaluate the mechanical properties of the collagen scaffold, we began by measuring how a single acellular lumen deformed under pressure. We recorded a series of confocal stacks and extracted the lumen cross-section at intraluminal pressures ranging from 100 to 300 Pa, given that the pressure at the upper surface of the gel was fixed at 100 Pa (upper panels in Fig. 2A; see Methods). This experiment showed that the vertical strain was ~10% for a pressure difference of 100 Pa, indicating that the elastic constant E was on the order of 1 kPa. Further, the contour of

the lumen was anisotropic, exhibiting greater expansion along the vertical axis compared to the horizontal, as seen in Fig. 2A or by plotting the horizontal and vertical axis derived from the fit of the lumen contour with an ellipse as a function of intraluminal pressure (Fig. 2B). This response was readily explained by poromechanics (upper panel of Fig. 2C), because in this single-channel configuration, fluid injection generates an interstitial pore pressure gradient oriented from the lumen to the top surface of the collagen gel. This gradient is associated to bulk collagen gel swelling predominantly in the vertical direction. Furthermore, the deformability was greater for low pressure inputs in comparison to higher ones, confirming the expected strain-stiffening behavior of collagen gels[24,25]. This response could be fitted using finite element simulations based on the Gent hyperelastic model, which is characterized by an exponential increase in elasticity with strain (black lines in Fig. 2B). Notably, the fitting of the anisotropy between the horizontal and vertical axis required considering compressibility in order to enable bulk poroelastic swelling. The compressibility typically corresponded to a Poisson coefficient on the order of 0.3 (Suppl. Fig. 3A).

Next, we investigated the expansion of a single MV and observed the persistence of a circular shape with increasing intraluminal pressure, as shown in the confocal micrographs (lower panels in Fig. 2A) and by plotting the variation of the vertical to horizontal axis ratio as a function of pressure (blue curve in Fig. 2C). Interestingly, finite element simulations in the elastic regime (lower panel of Fig. 2D) already capture the circular shape. The contrast between the elastic and poroelastic responses arises because, in poromechanics, interstitial pore pressure can propagate over long distances, whereas in purely elastic materials the influence of boundary conditions decays rapidly due to force-balance constraints. In fact, the switch to this elastic-like deformation is readily accounted for by the barrier function of the endothelial cell monolayer, which localizes the pressure gradient, hence impedes the bulk swelling of the hydrogel that accounts for the ovoidal deformation. This statement is demonstrated by conducting parametric simulations in the linear regime with different settings for the endothelial layer permeability, taking κ and E to $2 \cdot 10^{-14}$ m^2, based on our calibration[24], and 1 kPa, respectively, for the collagen gel, which show the circularization of the lumen and localization of the stress (Fig. 2E). Altogether, our data show the porohyperelastic response of collagen gels and the localization of the stress induced by impermeable endothelial cell monolayers.

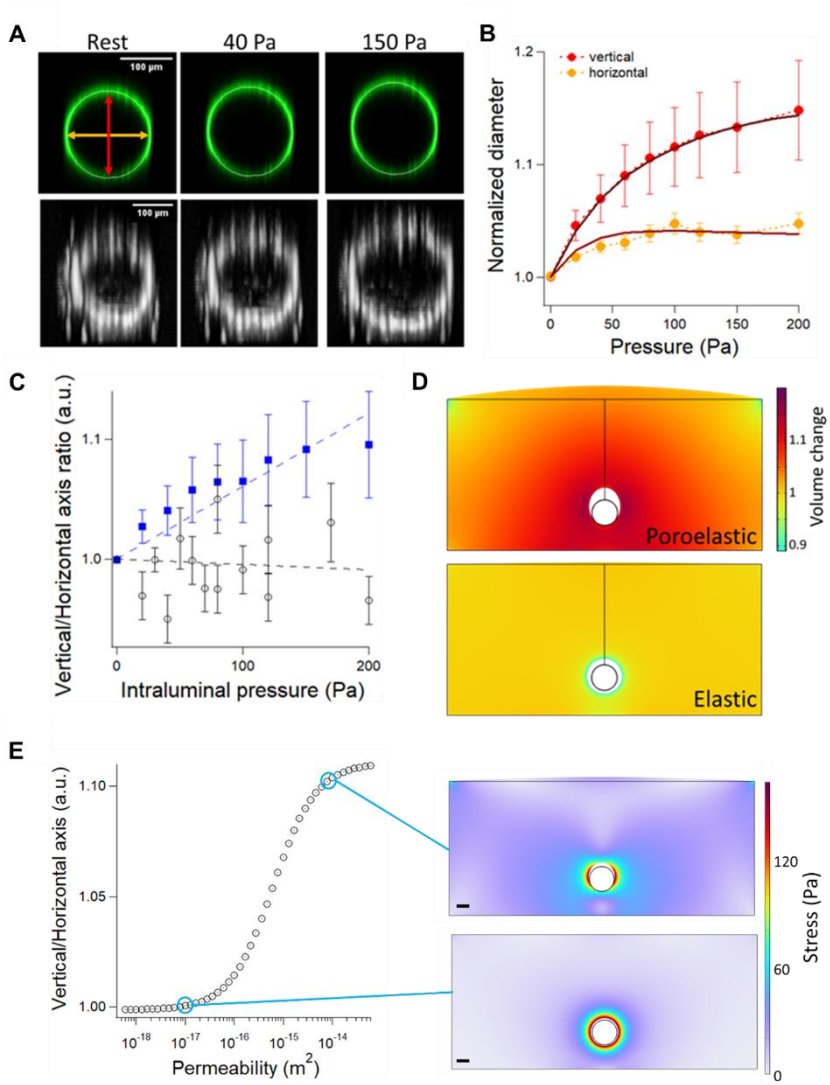

Figure 2 – Single lumen deformation in static conditions. (A) Cross-section of an acellular collagen scaffold and a microvessel for different intraluminal pressures (upper and lower panels, respectively). The collagen gel interface is labeled with 200 nm nanoparticles and the cell monolayer with the DNA intercalating dye Hoechst. **(B)** Variation of the vertical and horizontal axis of the acellular channel as a function of pressure (red and orange datasets, respectively, as indicated by the arrows in panel (A)). The black solid lines correspond to the fit of the data with numerical simulations based on the Gent porohyperelastic model a shear modulus of 250 Pa, a limiting extensibility parameter of 0.0085, and a compressibility of 1.5 kPa. **(C)** Variation of the vertical to horizontal axis ratio as a function of the intraluminal pressure for the acellular scaffold and for the MV (blue and black datasets, respectively). The dashed blue and black lines are guides to the eye based on linear fitting. **(D)** Finite element simulation of the deformation of a single channel in a poroelastic or an elastic material setting the elasticity to 1 kPa, the Poisson coefficient to 0.3, and the permeability to 2 10^{-14} m^2. **(E)** Variation of the vertical-to-horizontal axis ratio as a function of the endothelium permeability, as inferred from finite-element simulations. The two snapshots in the right present the result for the same endothelium elasticity of 1 kPa and two settings in permeability of 5 10^{-15} and 10^{-17} m^2. Scale bars = 100 µm.

Vasculature shows expansion-retraction asymmetry

We next examined how pulsatile actuation affects lumen deformation in both acellular and vascularized PIF chips (Fig. 3A, Suppl. Video 1,2). In acellular PIFs, artificial lumens (ALs)

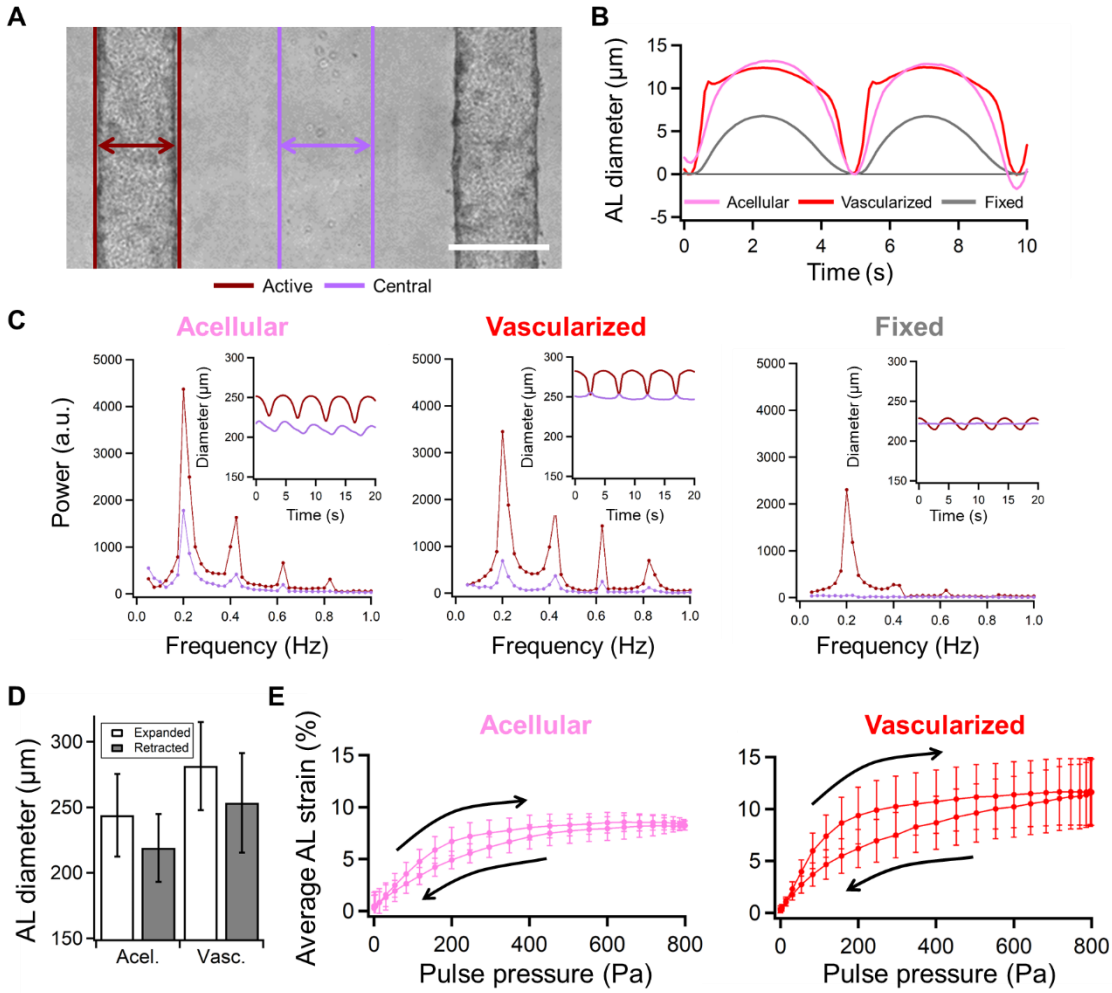

Figure 3 – Acellular lumen and microvessel deformation in PIF. (A) Depiction of diameter of the actuation MV and injection lumen (brown and purple lines, respectively) tracking strategy under bright field microscopy. Scale bar = 300 µm. **(B)** Strain response of the AL under pulsatile actuation in acellular PIF (pink), in vascularized PIF (red) and in PFA-fixed vascularized PIF (grey). **(C)** Fourier power spectrum analysis of the periodic signals shown in (B). **(D)** Average expanded and retracted AL diameter observed in acellular and vascularized PIFs. **(E)** Average acellular and vascularized AL response to a pressure cycle. Arrows indicate the strain response in expansion and retraction. Vascularized ALs exhibit faster initial expansion and larger maximum strain.

exhibited deformation cycles that deviated markedly from the sinusoidal input waveform. As illustrated by the pink curve of Fig. 3B, ALs displayed rapid expansion and retraction phases, interspersed with periods of minimal diameter variation—producing a waveform akin to a clipped sine wave. This behavior arises from the Gent-like hyperelastic properties of the collagen gel: the material remains compliant under low intraluminal pressure but stiffens as the load increases. Fourier analysis corroborated this observation, revealing high-order harmonics in the deformation signal (left panel, Fig. 3C). Notably, the Gent model parameters established in Fig. 2B accurately predicted both the deformation amplitude (~10%) and the clipped response pattern when applied

to PIF corss-section simulations (Suppl. Fig. 3B, C), in good agreement with experimental measurements.

The nonlinear deformation response was even more pronounced in vascularized PIFs, as evidenced by the plateaus interrupted by brief, rapid diameter changes (red curve, Fig. 3B). Fourier analysis of this response revealed a power spectrum dominated by high-order harmonics, with amplitudes significantly exceeding those observed in acellular lumens (middle panel, Fig. 3C). This result underscores the enhanced hyperelastic behavior of vascularized lumens compared to their acellular counterparts, and confirms previous observations of Gent-like response for MV models[26]. On average, vascularized ALs pulsated between larger expanded and retracted diameters than acellular Als (Fig. 3D) and also exhibited larger deformation amplitude per pulse (35 ± 14 vs 23 ± 7 μm for vascular and acellular PIFs, respectively).

Further analysis of the deformation dynamics highlighted an additional difference between the two systems. Acellular lumens exhibited nearly symmetrical expansion–retraction cycles, with only a 25% difference in the initial slopes of expansion and contraction (left graph, Fig. 3D). In contrast, MVs displayed a marked asymmetry: the initial expansion phase occurred 61% faster than the subsequent contraction (right graph, Fig. 3D). Notably, fixation of the endothelial cell monolayer abolished these characteristics, restoring a quasi-sinusoidal waveform (brown curve, Fig. 3B) and a Fourier power spectrum dominated by a single excitation peak. The fixing process also dampened deformation amplitudes, likely due to the increased stiffness induced by cellular fixation (right graph, Fig. 3C). Altogether, the asymmetry, combined with the pronounced nonlinear elasticity, appears to be a distinctive feature of live MVs.

MV pulsations induce strain accumulation and transient release in the collagen gel

Fourier analysis of the diameter signal in CLs (lavender curves, Fig. 3C) revealed greater deformation of the CL in acellular PIFs compared to vascularized systems, while also suggesting changes in strain spatial distribution between the two configurations. Similar trends were observed in the simulations (Suppl. Fig 3C). To quantify these differences, we measured a *proxy* of the collagen bulk deformation by tracking short-range (AL–CL) and long-range (AL–PL) luminal distance variations (Fig. 4A), capturing both lumen deformation and lateral displacements (Suppl. Video 1-4).

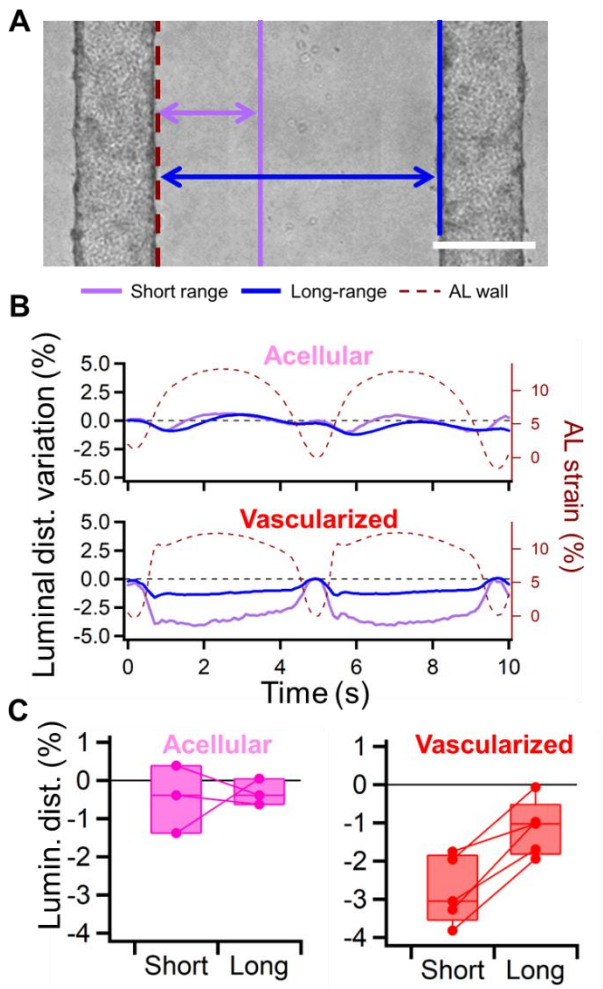

Figure 4 – Collagen gel bulk deformation in PIF. **(A)** Strategy for measuring intraluminal distance as a proxy for collagen gel strain at short or long range (lavender and blue arrows, respectively). Scale bar = 300 μm. **(B)** Intraluminal short- and long-range distance variation under pulsatile actuation in acellular PIF (top), vascularized PIF (bottom). **(C)** Average short and long-range bulk strain in acellular and vascularized PIF (left and right plots, respectively).

When applying constant pressure, acellular PIFs exhibited a delayed relaxation of AL and IL diameters (~5 s) consistent with Terzaghi poroelastic consolidation (diffusion-like kinetics, $\mu L^2/\kappa M$, with interstitial fluid viscosity μ = 1 mPa·s and lumen separation L ≈ 300 μm). In contrast, vascularized PIFs deformed nearly instantaneously, as the localized pressure gradient suppressed poroelastic consolidation (Suppl. Fig. 4A). This was translated to relaxed and sustained short-range collagen deformation for acellular and vascularized PIFs, respectively. Long-range deformation, on the other hand, increased until equilibrating in both cases, although much faster in acellular PIFs than in vascularized ones due to MV permeability delaying the pressure gradient diffusion through the collagen matrix (Suppl. Fig. 4B)

Switching to periodic pressure actuation, acellular PIFs displayed residual gel deformation (Fig. 4B, top panel), with short- and long-range strains effectively null, averaging -0.3 ± 0.7 and -0.2 ± 0.3 %, respectively (Fig. 4C, left panel). In vascularized PIFs, however, we clearly observed negative strain accumulation, punctuated by brief relaxation as MVs retracted to their smallest dimensions (Fig. 4B, bottom panel). Short-range strains were more pronounced than long-range strains (-2.0 ± 1.3% vs. -0.9 ± 0.7%, respectively; Fig. 4C, right panel). These behaviors were overall well recapitulated in the simulations, with the exception that acellular collagen strain became slightly positive instead (Suppl. Fig. 4C). In conclusion, collagen compression during pulsations arises because vascularization reduces long-range influence of pulsaitons, which instead cause rapid MV expansions that reduce AL–IL distances without greatly influencing the latter. Collectively, these findings demonstrate that vascularization introduces a complex

mechanical interplay, enabling transient strain accumulation and relaxation cycles in the collagen gel.

MV pulsations enhance solute transport

Next, we wished to investigate the effects of vascular pulsations in solute transport within the collagen hydrogel. We recorded a combination fluorescent-brightfield microscopy videos after injecting a tracer solution of FITC-dextran (Suppl. Fig. 5A) in the CL and monitored their general movement induced by typically one minute of AL actuation (Fig. 5A, see Methods). We selected a high–molecular-weight dextran (70 kDa) because its low diffusion coefficient in the collagen gel of 52 +/- 7 $\mu m^2/s$[27] results in marginal spreading within 2 min in the absence of pressure actuation (Supp. Fig. 5B).

We first characterized the spatial evolution of the dextran concentration profile using Gaussian fitting. In acellular devices, the amplitude and position of the center of the concentration front decreased and shifted toward the PL, respectively (Fig. 5A upper panel and 5B left panel). Photobleaching was quickly discarded as to why this happened because it was marginal in our diffusion experiments (Supp. Fig. 5B), leaving evacuation of the fluorophore through CL as the primary reason why fluorescent intensity quickly decreased, which was in some cases directly observed in our recordings (Suppl. Video 5). Additionally, in acellular PIFs the fluorescent signal steadily moved towards the PL, suggesting the existence of fluid evacuation through the PL. In vascularized PIFs, evacuation rates varied much more due to the intrinsic variability in permeability and deformability of MVs, but several key readouts remained consistent through our samples (Fig. 5A, lower panels): (i) tracers could not progress toward the PL because its barrier reduced the interstitial flow on this side of the PIF (note that the right arm of the distributions shown in the right panels of Fig. 5B remain almost at the same position), and (ii) pulsatile pressure enhanced the reduction of the fluorescence intensity signal more efficiently than constant pressure, as shown by the peak of the Gaussian of 0.20 and 0.36 after 20 s of pulsatile or constant pressure actuation, respectively (Fig. 5B). Hydraulic simulations of the PIF cross-section clearly showed that vasculature in the PL prevents any evacuation from happening in this lumen, redirecting flow towards the CL, opposite to what occurs in the acellular case (Suppl. Fig. 6A).

To combine the latter observation into a global readout that includes all samples, we computed the “normalized” clearance using the ratio I_{pulse}/I_{const} of the integral fluorescence intensity under pulsatile divide by constant pressure over time (Fig. 5C). Should this ratio increase, clearance would be more effectively with constant pressure than pulsatile pressure, and *vice-versa* if the

ratio decreases. On average, acellular samples showed a roughly constant ratio (I_{pulse}/I_{const} = 1.05 ± 0.20 after 20 s, n = 3), whereas tracer intensity evacuation occurred faster under pulsatile pressure in vascularized PIFs (I_{pulse}/I_{const}= 0.6 ± 0.1 after 20 s, n = 5).

To elucidate the link between enhanced tracer evacuation and MV pulsatile deformations, we tracked the progression of the fluorescent front in the AL–CL region across all experimental scenarios. Front position was defined as where fluorescent intensity was 30% of the maximum

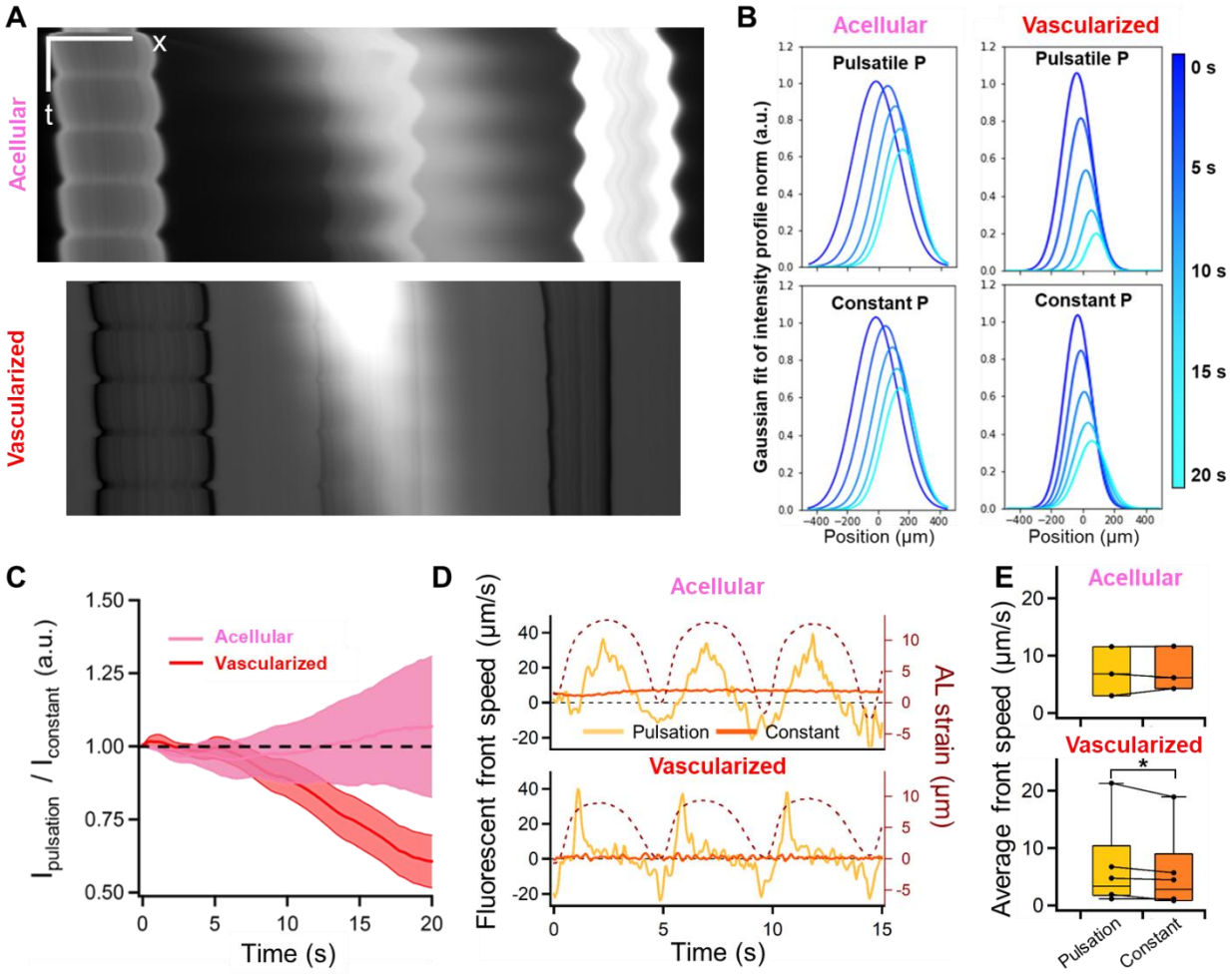

Figure 5 – Solute transport is enhanced by periodic actuation. **(A)** Kymographs of pulsating movies from acellular and vascularized PIFS. Acellular channels are coated with fluorescent nanoparticles for their visualization. Scale bars: Horizontal = 200 μm, Vertical = 50 s. **(B)** Gaussian fit of the fluorescent signal obtained from transport videos as a function of time, as indicated in the color scale. **(C)** Average fluorescence intensity ratio in pulsating vs constant pressure as a function of time for acellular or vascularized PIF (pink and red curves, respectively). **(D)** Fluorescent front displacement speed using constant or pulsatile pressure (yellow and orange curves, respectively) and the corresponding AL diameter represented with a red dashed line. The graph at the top corresponds to acellular PIF and that at the bottom to vascularized PIF. **(E)** General front speed graphs under constant and pulsatile pressure. The graph at the top corresponds to acellular PIF and that at the bottom to vascularized PIF. Vasculature produces significative higher displacement speed under pulsatile actuation rather than under constant actuation (n = 5, $p < 0.05$).

intensity of the Gaussian fitting (Fig. 5D). Front displacement rate was extracted as the temporal derivative of its position. We compared the front speed to the AL deformation cycles, both measured in the fixed referential of the microscope. In acellular systems, highest front velocity coincided with AL peak expansion, a hallmark of convection-dominated transport. Conversely, during AL retraction, the front velocity declined, occasionally becoming negative as the front was pulled backward. We can observe this effect in the kymograph in Fig. 5A, and simulations showed interstitial pressure stored within the collagen matrix even when AL pressure became 0, which would produce flow from the matrix into the AL (Suppl. Fig. 6B). The resulting average front velocity remained statistically comparable between pulsatile (6.4 ± 2.7 μm/s) and constant pressure (6.8 ± 1.9 μm/s) conditions (Fig. 5D, E, top panels). These values align qualitatively with predictions from Darcy's law (~5 μm/s), calculated using a hydraulic permeability $\kappa = 10^{-14}$ m², fluid viscosity μ = 1 mPa·s, and a pressure gradient of 400 Pa/mm. Collectively, these results demonstrate that solute transport in acellular PIFs is governed by convection, and that sinusoidal actuation yields transport outcomes equivalent to its time-averaged constant-pressure counterpart.

Comparatively, vascularized ALs produced fluorescent front displacement burst simultaneous to AL expansion, followed by slow progression of the front for the rest of the pulse (lower panel of Fig. 5E). During MV retraction, the front did not exhibit the coordinated motion observed in the acellular condition. Instead, negative front speed was also tied to MV complete retraction, which rapidly disappeared upon the following MV expansion. On the other hand, constant pressure applied to a MV produced at most one initial burst of front displacement, accounted by the first MV expansion, followed by slow constant fluorescent displacement. All of this together, produced on average a 1.3-flold faster tracer displacement by pulsatile actuation compared to constant actuation (Fig. 5F bottom), generalizable to 4.3 ± 3.6 μm/s under pulsations vs. 3.7 ± 2.7 μm/s under constant actuation.

Conclusions

In this study, we have investigated how MV pulsations can modify solute transport dynamics via an *in vitro* system coined the PIF device, which includes two parallel acellular or vascularized lumen and a tracer injection channel embedded in a collagen matrix. We first explored single lumen deformability in acellular and vascularized conditions, and demonstrate that the endothelial barrier function induces a localization of the strain at the vicinity of the MV. We then considered periodic pressure actuation in the PIF system, and observed the hyperporoelastic response of collagen gels associated to the generation of higher-order harmonics. Vascularized samples

enhanced this nonlinear response, further introduced an asymmetry in the expansion-retraction dynamics, and induced the storing of strain in the surrounding collagen matrix with a very transient release during MV retraction. These observations are qualitatively reproduced by numerical simulations of our PIF device assuming hyperelastic responses and linear properties for the permeability. We finally considered the impact of pulsations on solute transport. While transport in acellular PIFs was effectively equivalent with either constant or periodic pressure actuation, the intricate mechanical response of MVs associated to expansion/retraction asymmetry accelerated tracer displacement in periodic conditions in comparison to constant and purely-convective conditions. To explain this result, we propose a mechanism based on the accumulation of stress in the surrounding collagen bulk and the localization of the pressure gradient in the MV endothelial barrier that allows one-way movement of fluid out of the vasculature in a push-refill-push motion (Fig. 6). This analytical description of this mechanism appears as a technical challenge, especially as it is likely to rely on non-linear hydraulic MV properties, that we recently described based on the observation of a reinforcement of endothelial barrier function under mechanical strain[28].

Further improvement of our *in vitro* model may include faster actuation, a denser and stiffer extracellular matrix, and supportive perivascular cells in order to match *in vivo* conditions. The recreated vasculature is indeed oversimplified and the produced deformations are larger than physiological cues, given that brain microvasculature presents a diameter variation of ~1% per pulse[29]. Reproducing this deformation can be obtained by tuning the amplitude of the pressure actuation and by adjusting the stiffness of the extracellular matrix, which is less dense and stiff than *in vivo* tissues, even compared to the soft gray matter characterized by a Young modulus of

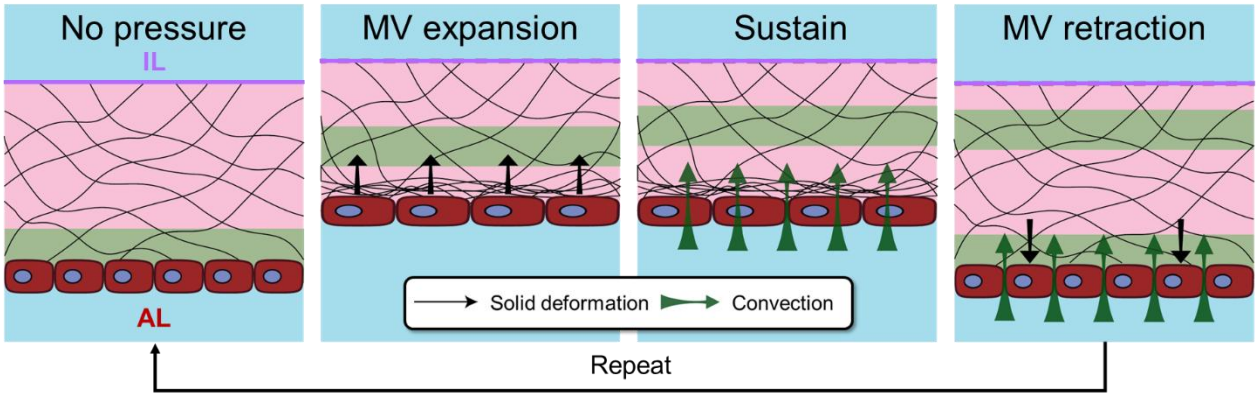

Figure 6 – Proposed MV pulsation-driven transport mechanism. Following a fraction of fluid (in green) near the AL, we suggest that MV expansion firstly strains the gel in the MV basal region. In the coplanar direction between the lumen, the strain in the gel pushes the fluid forward the IL. Then, the collagen gel remains strained while the residual permeation flow across the endothelium continues to convey the fluid. Lastly, the MV retracts slowly and the strain is relaxed. The unstrained barrier may favor fluid injection from the lumen to the basal layer, the motion of the initial fluid fraction being essentially null at this step. This phase lasts until the pulse pressure reaches zero and the cycle is re-initiated.

2 kPa[30]. Despite these differences, we believe that our observations may be useful to consolidate the role of vascular pulsatility on tissue homeostasis, particularly in the controversial case of the brain glymphatic model, in which IF movements seem to involve arterial push of fluid from the periarterial spaces towards the brain parenchyma[31,32]

Acknowledgements

This research was partly supported by WINGS-QSTEP (D.A.), LIMMS, and ARIM of the MEXT, Grant Number: JPMXP1223UT-0331. The authors thank Dr. Vincent Salles for his contributions on the use of the Keyence VHX-7000 microscope and Dr. Sylvie Lorthois and Dr. Matilde Fiori for their collaborative poroelastic modelling discussions.

METHODS

Cell culture: HUVEC

Human umbilical vein endothelial cells (HUVECs) (Lonza, Basel, Switzerland) were thawed and cultured in 60 mm diameter tissue culture dishes with EGM-2 endothelial cell culture medium (Lonza, Basel, Switzerland). HUVECs were expanded and passaged when they reach approximately 90% confluence (at 3-5 days) using 0.25% Trypsin - 0.5 mM EDTA. Culture medium was exchanged every other day and HUVEC culture was kept until passage number 7. HUVECs in suspension were directly injected into the two lateral channels of new PIF chips until complete covering with cells (Suppl. Fig 1) and let to mature for 3 days with medium change at the beginning of day 2. We assessed the barrier quality by monitoring the spatial redistribution of fluorescent dextran molecules of 70 kDa for each MV prior to their use in PIF settings (Suppl. Fig 2) [24]. The MV diffusive permeability spanned from 2 to 94×10^{-7} cm/s.

Silicone chip fabrication

Pieces of 3 mm thick clear silicone sheets (As One, Osaka, Japan) were placed in the laser cutter Etcher Laser Pro 30 W power (SmartDIYs, Yamanashi, Japan). The device pattern was engraved with a 100% laser power moving at a speed of 3500 mm/min one time (Suppl. Fig XX). Ash and debris were washed away under abundant water with a sponge and soap, and dried right after. The engraved silicone pieces were punched manually with biopsy punchers (Kai industries, Seki, Japan) of 5 mm and 3 mm in diameter to form the holes of the hydrogel chamber and reservoirs, respectively. Next, the silicone pieces together with a 1 mm thick silicone sheet (As One, Osaka, Japan) were exposed to air plasma for 1 min in a basic plasma cleaner (Harrick Plasma, Ithaca, NY, USA), and sequentially bonded. The resulting chip was eventually bonded to a 32 x 32 mm glass slide to form the final device (Suppl. Fig 1).

Double MV fabrication

Assembled devices and acupuncture needles (three per device) received the same surface treatment as seen in previous studies from the team[26]. BSA soaked needles were inserted into the device, crossing the central chamber completely. 60 µL of liquid type IA collagen (Nitta Gelatin, Osaka, Japan) was poured in the hydrogel cavity, and let to reticulate for 10 minutes at 37ºC. After reticulation, chips with the needles still inserted were kept at 37ºC submerged in sterile PBS for at least one day before use.

HUVECs were detached from a culture dish, and resuspended at a concentration of $4 \cdot 10^6$ cells/mL in culture medium supplemented with 3% dextran. This HUVEC suspension was directly injected in the lumen using a 30G needle attached to a pipette tip until the cell monolayer became homogeneous (Suppl. Fig. 1). This process was repeated for the second lumen. Devices were then put to rest for 10 minutes in the incubator, after which the middle needle was removed, and 0.5 mL of fresh culture medium was poured on top of the PIF device. Culture medium was renewed every other day until pressure experiments were conducted.

For each vascularized PIF device, we determined the MV diffusive permeability for both vasculatures using the previously published protocol[25]. It consisted in loading a solution containing 70 kDa FITC-conjugated dextran (Sigma-Aldrich, Missouri, USA) in the lumen, and monitoring the diffusion-driven fluorescence spatial redistribution of this dye by confocal microscopy. By measuring the flux of tracers crossing the endothelial barrier and the concentration difference between the basal and luminal sides of the MV, we could compute their ratio to evaluate the diffusive permeability[27]. PIF devices were finally thoroughly rinsed with sterile PBS.

3D printed pressure control interface and transport experiment

Pressure interface pieces were designed using Fusion360 software. The digital models were 3D printed using SLA Elegoo Mars 3pro 3D printer in clear resin Expert material (W-64C05, NSS co ltd.). Slicing of the pieces was set at 50 µm with 2.5 seconds of exposure per layer. Note that 3D pieces were biocompatibilized by secondary curing overnight under 36W UV light with no thermal treatment, resulting in total cell survivability using Cell Counting Kit-8 (Dojindo Laboratories, Kumamoto, Japan; Suppl Fig 2). This pressure interface was connected to three independent pressure controllers (MFCS, Fluigent, Paris; Suppl. Fig. 2) and mounted on the PIF chip using screws and O-rings for waterproofing. Once sealed, all three pressure channels were set to 100 Pa until experiments started. FITC-conjugated 70 kDa dextran was conveyed into CL by manually opening a valve for a few seconds just before the experiment (Suppl. Fig. 5A). Once the fluorophore was detected in the totality of the CL, the valve was closed and we started pressure actuation in the AL.

Microscopies

Diffusion through the MV barrier assays were recorded by the confocal laser scanning microscope LMS-700 (Carl-Zeiss, Oberkochen, Germany) at 20x. Transport experiments were recorded by AXIO observer Z1 microscope (Carl Zeiss, Oberkochen, Germany) paired with a Zyla 5.5 sCMOS

high-speed camera (Andor, Belfast, United Kingdom) focusing on the equatorial plane of the MVs at 5× of magnification. MV deformation areas were analyzed to determine the MV diameter on each frame of the recording, as described in ref. Bancaud Lab Chip 2025. The motion of fluorescent tracers was analyzed by a custom-made python code that averaged and normalized the intensity profile along the recorded area and fitted it with a gaussian function. From each gaussian fit, total dextran signal integral and dextran front position at 30% of the maximum were extracted. For silicone laser-engraved profile measurements, we used a Keyence VHX-7000 microscope (Keyence, Osaka, Japan) (Suppl. Fig. 1).

COMSOL simulations

The 2D cross-section of PIF chips was modelled in COMSOL Multyphysics software (COMSOL, Stockholm, Sweden). We used the module for Darcy's permeability and solid mechanics intertwined in the poroelasticity multiphysics module. The parameters for collagen gels were set according to density = 1000 kg/m^3, fluid viscosity = 10^{-3} Pa·s, porosity = 0.99, permeability = $2\cdot10^{-14}$ m^2, Young modulus = 1000 Pa, Poisson's ratio = 0.3. The parameters for microvessels were set to: density = 1000 kg/m^3, fluid viscosity = 10^{-3} Pa·s, porosity = 0.01, permeability = 10^{-17} m^2 or variable, Young modulus = 5 kPa or variable, Poisson's ratio = 0.3. Active pressure was set to 500 Pa, while injection and passive were set to 100 Pa. We also implemented to Gent model to model the nonlinear elastic properties of collagen gels.

Cross-section of PIF chip was modelled in COMSOL Multyphysics software (COMSOL, Stockholm, Sweden). Collagen parameters: density = 1000 kg/m^3, viscosity = 10^{-3} Pa·s, porosity = 0.99, permeability = $3\cdot10^{-14}$ m^2, Young modulus = 500 Pa, Poisson's ratio = 0.1. Microvessel parameters: density = density = 1000 kg/m^3, viscosity = 10^{-3} Pa·s, porosity = 0.01, permeability = 10^{-17} m^2, Young modulus = 5 kPa, Poisson's ratio = 0.3. Active pressure was set to 500 Pa, while injection and passive were set to 100 Pa. Darcy's lay and solid mechanics intertwined in the poroelasticity multiphysics module.

REFFERENCES

1. Michel, C. C., Woodcock, T. E. & Curry, F.-R. E. Understanding and extending the Starling principle. *Acta Anaesthesiol. Scand.* **64**, 1032–1037 (2020).
2. Dessalles, C. A., Ramón-Lozano, C., Babataheri, A. & Barakat, A. I. Luminal flow actuation generates coupled shear and strain in a microvessel-on-chip. *Biofabrication* **14**, (2021).
3. Wiig, H. & Swartz, M. A. Interstitial Fluid and Lymph Formation and Transport: Physiological Regulation and Roles in Inflammation and Cancer. *Physiol. Rev.* **92**, 1005–1060 (2012).
4. Thompson, B., Gaitatzis, K., Janse de Jonge, X., Blackwell, R. & Koelmeyer, L. A. Manual lymphatic drainage treatment for lymphedema: a systematic review of the literature. *J. Cancer Surviv.* **15**, 244–258 (2021).
5. Cohen, S. R., Payne, D. K. & Tunkel, R. S. Lymphedema. *Cancer* **92**, 980–987 (2001).
6. Iliff, J. J. *et al.* A Paravascular Pathway Facilitates CSF Flow Through the Brain Parenchyma and the Clearance of Interstitial Solutes, Including Amyloid β. *Sci. Transl. Med.* **4**, 147ra111-147ra111 (2012).
7. Jessen, N. A., Munk, A. S. F., Lundgaard, I. & Nedergaard, M. The Glymphatic System: A Beginner's Guide. *Neurochem. Res.* **40**, 2583–2599 (2015).
8. Alcaide, D., Cacheux, J., Bancaud, A., Muramatsu, R. & T. Matsunaga, Y. Solute transport in the brain tissue: what are the key biophysical parameters tying in vivo and in vitro studies together? *Biomater. Sci.* **11**, 3450–3460 (2023).
9. Bohr, T. *et al.* The glymphatic system: Current understanding and modeling. *iScience* **25**, (2022).
10. Asgari, M., de Zélicourt, D. & Kurtcuoglu, V. Glymphatic solute transport does not require bulk flow. *Sci. Rep.* **6**, 38635 (2016).
11. Zhang, L. Solute transport in cyclic deformed heterogeneous articular cartilage. *Int. J. Appl. Mech.* **03**, 507–524 (2011).

12. DiDomenico, C. D., Xiang Wang, Z. & Bonassar, L. J. Cyclic Mechanical Loading Enhances Transport of Antibodies Into Articular Cartilage. *J. Biomech. Eng.* **139**, (2016).

13. Bonassar, L. J. *et al.* The effect of dynamic compression on the response of articular cartilage to insulin-like growth factor-I. *J. Orthop. Res.* **19**, 11–17 (2001).

14. Gardiner, B. *et al.* Solute transport in cartilage undergoing cyclic deformation. *Comput. Methods Biomech. Biomed. Engin.* **10**, 265–278 (2007).

15. Mauck, R. L., Hung, C. T. & Ateshian, G. A. Modeling of Neutral Solute Transport in a Dynamically Loaded Porous Permeable Gel: Implications for Articular Cartilage Biosynthesis and Tissue Engineering. *J. Biomech. Eng.* **125**, 602–614 (2003).

16. Urciuolo, F., Imparato, G. & Netti, P. A. Effect of dynamic loading on solute transport in soft gels implication for drug delivery. *AIChE J.* **54**, 824–834 (2008).

17. Scheidegger, A. E. General theory of dispersion in porous media. *J. Geophys. Res. 1896-1977* **66**, 3273–3278 (1961).

18. Fiori, M., Pramanik, S. & MacMinn, C. W. Solute transport due to periodic loading in a soft porous material. *J. Fluid Mech.* **1009**, A15 (2025).

19. Taylor, G. I. Dispersion of soluble matter in solvent flowing slowly through a tube. *Proc. R. Soc. Lond. Math. Phys. Sci.* **219**, 186–203 (1953).

20. Aris, R. On the dispersion of a solute in a fluid flowing through a tube. *Proc. R. Soc. Lond. Math. Phys. Sci.* **235**, 67–77 (1956).

21. Gouze, P., Puyguiraud, A., Porcher, T. & Dentz, M. Modeling Longitudinal Dispersion in Variable Porosity Porous Media: Control of Velocity Distribution and Microstructures. *Front. Water* **3**, (2021).

22. Pauty, J. *et al.* A Vascular Endothelial Growth Factor-Dependent Sprouting Angiogenesis Assay Based on an In Vitro Human Blood Vessel Model for the Study of Anti-Angiogenic Drugs. *eBioMedicine* **27**, 225–236 (2018).

23. Kenyon, D. E. A mathematical model of water flux through aortic tissue. *Bull. Math. Biol.* **41**, 79–90 (1979).

24. Cacheux, J. *et al.* Asymmetry of tensile versus compressive elasticity and permeability contributes to the regulation of exchanges in collagen gels. *Sci. Adv.* **9**, eadf9775 (2023).

25. Motte, S. & Kaufman, L. J. Strain stiffening in collagen I networks. *Biopolymers* **99**, 35–46 (2013).

26. Salipante, P. F., Hudson, S. D. & Alimperti, S. Blood vessel-on-a-chip examines the biomechanics of microvasculature. *Soft Matter* **18**, 117–125 (2021).

27. Alcaide, D. *et al.* Laminin and hyaluronan supplementation of collagen hydrogels enhances endothelial function and tight junction expression on three-dimensional cylindrical microvessel-on-a-chip. *Biochem. Biophys. Res. Commun.* **724**, 150234 (2024).

28. Bancaud, A. *et al.* Intraluminal pressure triggers a rapid and persistent reinforcement of endothelial barriers. *Lab. Chip* **25**, 2061–2072 (2025).

29. Guo, F. *et al.* Assessing cerebral microvascular volumetric with high-resolution 4D cerebral blood volume MRI at 7 T. *Nat. Cardiovasc. Res.* **4**, 1424–1438 (2025).

30. Budday, S. *et al.* Mechanical properties of gray and white matter brain tissue by indentation. *J. Mech. Behav. Biomed. Mater.* **46**, 318–330 (2015).

31. Hablitz, L. M. & Nedergaard, M. The glymphatic system. *Curr. Biol.* **31**, R1371–R1375 (2021).

32. Nozaleda, G. L., Coenen, W., Haughton, V. & Sánchez, A. L. Arterial pulsations and transmantle pressure synergetically drive glymphatic flow. *Sci. Rep.* **15**, 13798 (2025).